Monthly Notices
of the
ROYAL ASTRONOMICAL SOCIETY

Mon. Not. R. Astron. Soc. **401,** 533–546 (2010) doi:10.1111/j.1365-2966.2009.15678.x

# Deep Gemini/GMOS imaging of an extremely isolated globular cluster in the Local Group

A. D. Mackey,[1⋆] A. M. N. Ferguson,[1] M. J. Irwin,[2] N. F. Martin,[3] A. P. Huxor,[4] N. R. Tanvir,[5] S. C. Chapman,[2] R. A. Ibata,[6] G. F. Lewis[7] and A. W. McConnachie[8]

[1]*Institute for Astronomy, University of Edinburgh, Royal Observatory, Blackford Hill, Edinburgh EH9 3HJ*
[2]*Institute of Astronomy, University of Cambridge, Madingley Road, Cambridge CB3 0HA*
[3]*Max-Planck-Institut für Astronomie, Königstuhl 17, D-69117 Heidelberg, Germany*
[4]*Department of Physics, University of Bristol, Tyndall Avenue, Bristol BS8 1TL*
[5]*Department of Physics and Astronomy, University of Leicester, University Road, Leicester LE1 7RH*
[6]*Observatoire Astronomique, Université de Strasbourg, CNRS, 11, rue de l'Université, F-67000 Strasbourg, France*
[7]*Institute of Astronomy, School of Physics, A29, University of Sydney, NSW 2006, Australia*
[8]*NRC Herzberg Institute for Astrophysics, 5071 West Saanich Road, Victoria, British Columbia V9E 2E7, Canada*

Accepted 2009 September 5. Received 2009 September 1; in original form 2009 June 9

## ABSTRACT

We report on deep imaging of a remote M31 globular cluster, MGC1, obtained with Gemini/GMOS. Our colour–magnitude diagram for this object extends ∼5 mag below the tip of the red-giant branch and exhibits features consistent with an ancient metal-poor stellar population, including a long, well-populated horizontal branch. The red-giant branch locus suggests MGC1 has a metal abundance [M/H] ≈ −2.3. We measure the distance to MGC1 and find that it lies ∼160 kpc in front of M31 with a distance modulus $\mu = 23.95 \pm 0.06$. Combined with its large projected separation of $R_{\rm p} = 117$ kpc from M31, this implies a deprojected radius of $R_{\rm gc} = 200 \pm 20$ kpc, rendering it the most isolated known globular cluster in the Local Group by some considerable margin. We construct a radial brightness profile for MGC1 and show that it is both centrally compact and rather luminous, with $M_V = -9.2$. Remarkably, the cluster profile shows no evidence for a tidal limit and we are able to trace it to a radius of at least 450 pc, and possibly as far as ∼900 pc. The profile exhibits a power-law fall-off with exponent $\gamma = -2.5$, breaking to $\gamma = -3.5$ in its outermost parts. This core-halo structure is broadly consistent with expectations derived from numerical models, and suggests that MGC1 has spent many gigayears in isolation.

**Key words:** globular clusters: general – galaxies: individual: M31.

## 1 INTRODUCTION

Cosmological models of structure formation predict that galaxies are built up via the hierarchical accretion and merger of many smaller subsystems over time. It is expected that the signatures of these galaxy assembly processes may be seen in the outskirts of present-day large galaxies where dynamical time-scales are very long. Globular clusters, as luminous compact objects that are found out to distant radii in the haloes of massive galaxies, are thus potentially extremely useful probes of galaxy formation. This is especially the case for systems beyond a few Mpc where globular clusters are often the only accessible tracers of ancient stellar populations.

In terms of testing and refining these ideas, galaxies in the Local Group play a central role. They are close enough that their various components, including individual globular clusters, may be studied in detail as resolved stellar populations. M31 is of particular significance as it is the nearest large galaxy to our own, and possesses the most extensive globular cluster system in the Local Group. This galaxy has been targeted by a number of wide-field imaging surveys in recent years and these have revealed a wealth of low-brightness substructure in its outer regions (e.g. Ibata et al. 2001; Ferguson et al. 2002; Ibata et al. 2007; McConnachie et al. 2009) as well as many new members of its halo globular cluster system, extending to very large radii (e.g. Huxor et al. 2005; Mackey et al. 2006, 2007; Huxor et al. 2008).

Although the M31 globular cluster system shares many similarities with that of the Milky Way, as the sample of outer halo M31 globular clusters has grown and been studied in more detail over the past few years several clear differences have emerged. Among these are the existence in the M31 system of very extended yet still rather luminous clusters (Huxor et al. 2005; Mackey et al. 2006; Huxor et al. 2008) that do not seem to have matching counterparts in the Milky Way, and indications that M31 may possess many more very

⋆E-mail: dmy@roe.ac.uk

luminous compact globular clusters in its outer regions than does the Milky Way (e.g. Mackey et al. 2007; Huxor et al. 2009). The origin of these distinctions is not yet clear but it has been speculated that they may reflect differences in the formation and/or accretion histories of the Milky Way and M31. It is therefore of considerable interest to obtain as much additional information as possible about the remote globular cluster system in M31.

One of the most intriguing newly found objects in the M31 halo is a bright globular cluster discovered by Martin et al. (2006) in survey observations from the MegaCam imager on the Canada–France–Hawaii Telescope (CFHT). The cluster lies at $\alpha = 00{:}50{:}42.45$, $\delta = +32{:}54{:}58.70$ (J2000.0), or roughly $\sim 8\overset{\circ}{.}5$ from the centre of M31.[1] Adopting the standard distance to M31 of $\approx$780 kpc (McConnachie et al. 2005), this angular separation corresponds to a projected radius of $R_{\rm p} = 117$ kpc, placing the new globular cluster among the most remote such objects yet known in the M31 system and, indeed, in the Local Group as a whole. Following the nomenclature adopted in the latest version (V3.5) of the Revised Bologna Catalogue (RBC) of M31 globular clusters (Galleti et al. 2007), we hereafter refer to this object as MGC1.

Martin et al. (2006) used their CFHT/MegaCam discovery imagery to measure a few characteristics of the cluster. They found it to be a compact, luminous object with half-light radius $r_{\rm h} \sim 2.3 \pm 0.2$ pc and absolute integrated magnitude $M_V = -8.5 \pm 0.3$. Their colour–magnitude diagram (CMD) showed a well-populated red-giant branch (RGB), and a probable horizontal branch (HB) near their faint detection limit. Isochrone fitting implied a metal abundance [Fe/H] $\approx -1.3$. Most intriguingly, the observed brightness of the tip of the RGB, along with that of the putative HB, suggested that MGC1 may lie considerably closer than M31, meaning that the cluster may be extremely isolated indeed with a deprojected galactocentric radius of $175 \pm 55$ kpc.

Two groups have published radial velocities for MGC1: Galleti et al. (2007) obtained $v_{\rm r} = -312 \pm 17$ km s$^{-1}$ from low-resolution spectroscopy, while Alves-Brito et al. (2009) measured $v_{\rm r} = -354.7 \pm 2.2$ km s$^{-1}$ from a high-resolution Keck spectrum. These measurements are consistent with the systemic velocity of M31 ($v_{\rm r} = -300$ km s$^{-1}$), suggesting that MGC1 is a bona fide member of M31's outer halo globular cluster system. In this regard, it is of considerable significance as very few such objects have yet been discovered – there are only three other known globular clusters in M31 with $R_{\rm p} \gtrsim 70$ kpc (Mackey et al. 2007; Huxor et al. 2008). Indeed, there are also very few individual halo stars that have been identified at projected radii comparable to that of MGC1 (e.g. Kalirai et al. 2006; Chapman et al. 2008).

In this paper, we present results from deep Gemini follow-up imaging of this intriguing cluster, with the particular goals of (i) obtaining an accurate distance measurement in order to understand properly its position in the M31 system, (ii) obtaining a precise estimate of its metal abundance and (iii) making a thorough analysis of its structure.

## 2 OBSERVATIONS AND DATA REDUCTION

### 2.1 Imaging and photometry

Our deep imaging of MGC1 was carried out in queue mode on the night of 2007 October 13 using the Gemini Multi-Object Spectrograph (GMOS) at the 8.1-m Gemini North telescope on Mauna Kea, Hawaii. The data were obtained in clear, photometric conditions and under excellent seeing (0.4– 0.5 arcsec). The GMOS imager (Hook et al. 2004) is comprised of three adjacent $2048 \times 4096$ pixel CCDs separated by gaps of $\sim$2.8 arcsec, and has a field of view (which does not cover the full CCD package) of $5.5 \times 5.5$ arcmin$^2$. To take advantage of the high-quality conditions, we employed unbinned imaging, resulting in a plate scale of 0.0727 arcsec pixel$^{-1}$. We obtained our observations in the GMOS $g'$, $r'$ and $i'$ filters, which are very similar to the $g$, $r$ and $i$ filters used by the Sloan Digital Sky Survey (SDSS). Details of the SDSS photometric system may be found in Fukugita et al. (1996). We took six images per filter, arranged in a $3 \times 2$ dither pattern with a step size of 5 arcsec designed to eliminate the gaps between the CCDs and provide continuous coverage of our field. Exposure durations were 400 s per image for the $r'$ and $i'$ filters and 600 s per image for the $g'$ filter.

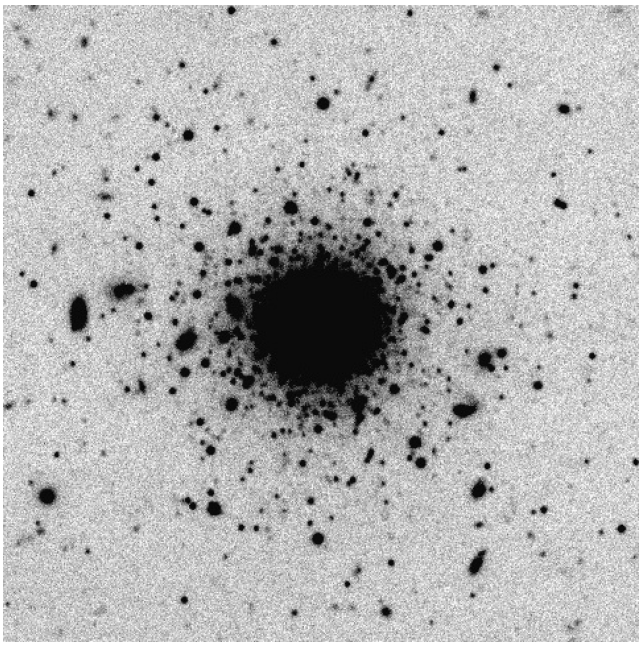

**Figure 1.** Central $70 \times 70$ arcsec$^2$ region of our combined 2400s $i'$-band GMOS image, showing MGC1. Stellar objects in this image have a FWHM $\approx$6.2 pixels or 0.45 arcsec. North is towards the top of the image and east is to the left.

We reduced our data using the GMOS reduction package in IRAF. Appropriate bias and flat-field images obtained as part of the standard GMOS baseline calibrations were downloaded from the Gemini science archive and then applied to each exposure using the GIREDUCE task. The three CCD frames in a given exposure were next mosaicked into a single frame using the GMOSAIC task, and the six mosaicked frames for a given filter were then combined into a single image using the IMCOADD task.

Fig. 1 shows the central $70 \times 70$ arcsec$^2$ region of our combined 2400s $i'$-band image. Stellar objects in this image have a full width at half-maximum (FWHM) $\approx$ 6.2 pixels, or 0.45 arcsec, and the outer region of MGC1 is clearly resolved into stars. The inner part of the cluster is unresolved, but, as described below, the images none the less contain a sufficient number of individual cluster members to produce a well-populated CMD.

We performed photometric measurements on our combined images using the stand-alone versions of DAOPHOT II and ALLSTAR II (Stetson 1987). Because of the crowded nature of the region of interest, full point-spread function (PSF) fitting photometry was

[1] Assumed to be at $\alpha = 00{:}42{:}44.31$, $\delta = +41{:}16{:}09.4$ (J2000.0).

necessary. For each combined image, we used DAOPHOT II to conduct a first pass of object detection, and selected ∼75 relatively bright, isolated stars to construct an initial PSF. Some experimentation showed that the best fit was obtained by selecting a Gaussian PSF model and allowing quadratic variation across the field of view. Stars with an error in their fit more than three times the average were removed from the list, and the PSF redefined. After iterating until convergence, at which point there were typically still ∼50–60 stars defining the PSF model, we used ALLSTAR to subtract from the image all stars in close proximity to those used to construct the PSF. The now-isolated PSF stars on this subtracted image were used to recalculate and further refine the PSF model. Next, we used ALLSTAR to apply this model to the original image and subtract all known stars. This subtracted image was then run through DAOPHOT in order to find faint objects missed in the first detection pass. We then took the original image and our final PSF model and used ALLSTAR to perform photometric measurements on the complete list of detected objects.

In order to eliminate non-stellar objects or objects with poor photometry, we passed the resulting list of measurements through several quality filters based on information calculated during the PSF fitting. Specifically, we filtered objects by the $\chi^2$ of their fit, their estimated photometric error, and their measured sharpness relative to the PSF model. To define suitable ranges in these parameters for well-measured point sources we selected all objects in an annulus of radius 12–40 arcsec centred on the cluster, corresponding to the region populated almost exclusively by cleanly resolved member stars. These objects defined clear, narrow loci in terms of $\chi^2$, photometric error and sharpness as functions of magnitude in each of the three filters, which we used to prune the final list of detections across the full field of view.

### 2.2 Photometric calibration

In addition to observing our target field, we also obtained imaging of photometric standard stars in one equatorial field, around star SA 92−249 (Landolt 1992). This imaging was conducted through all three filters immediately after the observations of our primary field were complete. We took two exposures per filter, with durations of 4, 3 and 2 s each in $g', r'$, and $i'$, respectively. An identical reduction process to that followed for the primary imaging was applied to the observations of our photometric standards to produce one mosaicked, combined image per filter. We then used the stand-alone version of DAOPHOT II to perform aperture photometry on the standard stars in these combined images, using an aperture equal in radius to that for the PSF models we used to obtain photometric measurements from the main cluster images.

In all, six photometric standard stars were covered by the GMOS field of view. Unfortunately, however, we could only obtain accurate photometric measurements for four of these – one star was completely vignetted by the GMOS On-Instrument Wavefront Sensor (OIWFS), which facilitates precise guiding and use of the telescope's active optics system, while a second star fell on the gap between the CCDs in half the images.

Our standard field lies within the SDSS footprint, however, the stars are sufficiently bright that they are flagged as saturated in the SDSS catalogue. We therefore employed an alternative method of obtaining their SDSS *g*-, *r*- and *i*-band AB-magnitudes, by transforming the Landolt (1992) Johnson–Kron–Cousins *BVRI* measurements using the relations listed on the SDSS Data Release 7 (DR7) website.[2] Specifically, we used inverted versions of Lupton's *ugriz* to *BVRI* transformations,

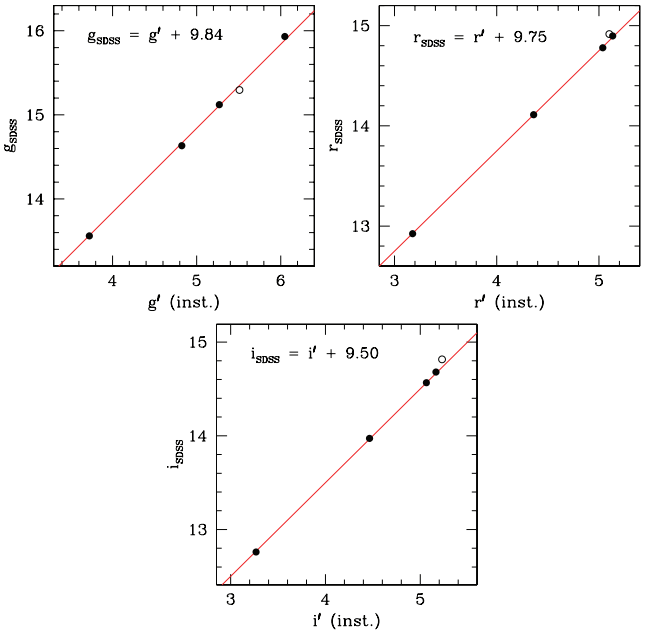


**Figure 2.** Transformations from GMOS instrumental magnitudes to SDSS AB magnitudes derived from the observed photometric standards. The four stars with complete measurements are marked as solid points, while the star which fell on the CCD gap in half the images is an open point.

$$\begin{aligned} g &= 0.6489\,B + 0.3511\,I - 0.1460, \\ r &= 1.3088\,R - 0.3088\,I + 0.0704, \\ i &= 0.2570\,R + 0.7430\,I + 0.3208. \end{aligned} \quad (1)$$

The other alternative transformations listed on the DR7 webpage, in particular those of Jester et al. (2005), Bilir, Karaali & Tunçel (2005) and Jordi, Grebel & Ammon (2006) give matching *gri* magnitudes for our standards to within a few × 0.01 mag. Therefore, the selection of any of these sets of relations would not significantly alter our derived photometric calibration.

Fig. 2 shows the relationship between our measured GMOS instrumental $g', r'$ and $i'$ magnitudes for the standard stars, and their derived SDSS *gri* AB-magnitudes. The instrumental magnitudes as plotted have been corrected to the exposure times of the three respective combined cluster images. In each panel, the star marked with an open circle was that which fell on the gap between the CCDs in half the images. We did not use our measurements for this star when calculating the best-fitting transformations. From Fig. 2, the relationships between $g'$ $r'$ $i'$ and *gri* are well described by a simple zero-point shift. We determined the best-fitting calibration via linear regression,

$$\begin{aligned} g &= g' + 9.84, \\ r &= r' + 9.75, \\ i &= i' + 9.50. \end{aligned} \quad (2)$$

Formal (random) uncertainties on these zero-point shifts from the linear regression are typically ±0.02 mag. Even so, the above transformations were derived using only four stars which do not span a particularly large range in colour [$0.45 \leq (g - i) \leq 1.35$], meaning

[2] http://www.sdss.org/dr7/algorithms/sdssUBVRITransform.html

that it was impossible for us to determine colour terms for equation (2). Jorgensen (2009) has demonstrated that small colour terms are expected in transformations to the SDSS photometric systems for all GMOS-N filters, and has used a large number of standard star observations to derive these corrections. Unfortunately, her photometric calibration and colour terms are valid only for data obtained prior to 2004 November when the main mirror of Gemini North was recoated with silver in place of aluminium, and so we cannot use them directly for our MGC1 observations. None the less, we expect them to give some indication of the size of the systematic errors introduced into our photometric calibration by not including any colour terms in equation (2).

Our CMDs show that stars in MGC1 span $-0.2 \lesssim (g-r) \lesssim 1.4$ and $-0.4 \lesssim (g-i) \lesssim 1.7$ (see Section 3.1). The appropriate colour-term corrections to *gri* magnitudes from Jorgensen (2009) are then

$$\begin{aligned}
\Delta g_1 &= 0.066(g-r) - 0.037, \\
\Delta g_2 &= 0.035(g-i) - 0.029, \\
\Delta r_1 &= 0.027(g-r) - 0.016, \\
\Delta r_2 &= 0.017(g-i) - 0.015, \\
\Delta i_1 &= 0.039(g-r) - 0.020, \\
\Delta i_2 &= 0.025(g-i) - 0.018,
\end{aligned} \tag{3}$$

where the two corrections $\Delta m_1$ and $\Delta m_2$ for a given filter may be calculated independently. Over the range of colours spanned by cluster members, these would correspond to systematic offsets in our SDSS magnitudes of $-0.04 \lesssim \Delta g \lesssim 0.04$, $-0.02 \lesssim \Delta r \lesssim 0.02$, and $-0.03 \lesssim \Delta i \lesssim 0.03$, and in our SDSS colours of $-0.02 \lesssim \Delta(g-r) \lesssim 0.02$ and $-0.01 \lesssim \Delta(g-i) \lesssim 0.01$. Such uncertainties are comparable in size to the formal random uncertainties on our zero-points (equation 2). As such, we are confident that in what follows our analysis and conclusions are largely unaffected by the fact that we did not include colour terms in our photometric calibration. For completeness, where appropriate we explicitly make note of the effects these small systematic offsets may have on our measurements of MGC1.

## 3 ANALYSIS OF THE CMD

### 3.1 General properties

Our final $(g, r)$ and $(g, i)$ CMDs are presented in Fig. 3. The upper panels show all detected objects which passed successfully through the quality filter we described in Section 2.1, while the lower panels show the subset of those objects which lie in the projected radial range 12–40 arcsec from the centre of MGC1. We determined these radial limits empirically, to exhibit the best-defined cluster sequences with minimal degradation due to crowding or background contamination. The lower panels also show the typical photometric uncertainties as functions of magnitude.

The cluster sequences are clearly visible in the upper panels in Fig. 3 as are several contaminating populations. To the red side of the CMDs, at $(g-r) \gtrsim 1.2$ and $(g-i) \gtrsim 1.6$, lies the sequence due to Galactic disc dwarfs; this is most prominent in the $(g, r)$ CMD. Also evident are a few members of the Galactic halo [e.g. at $(g-i) \lesssim 1.0$ and $i \lesssim 22.5$] and a significant number of faint unresolved galaxies [which have $0.0 \lesssim (g-i) \lesssim 1.4$ and $i \gtrsim 25.0$]. In the lower panels, which cover only a limited area on the sky, objects from these populations are almost completely absent.

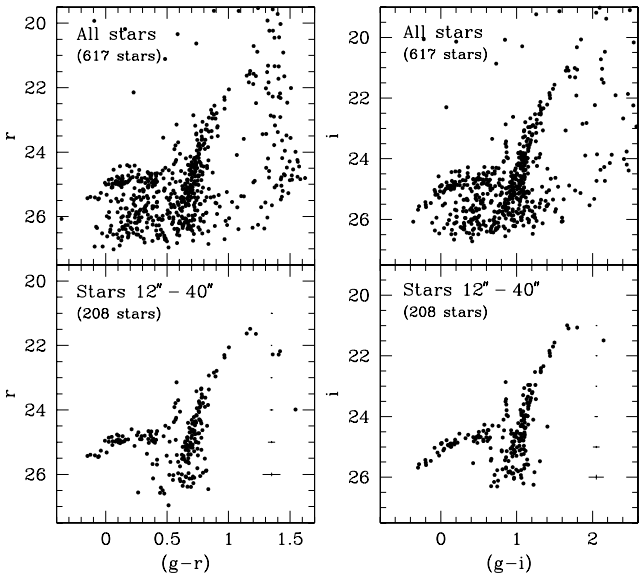


**Figure 3.** Final $(g, r)$ and $(g, i)$ CMDs for the full GMOS frame (upper panels) and for an annulus spanning the radial range 12–40 arcsec centred on MGC1 (lower panels). Typical photometric uncertainties are marked in the lower panels.

The cluster itself possesses a well-populated steep RGB and a HB that extends far to the blue. Our photometry reaches ∼1.5 mag below the HB, meaning that this feature is clearly isolated on the CMD. There are no large gaps along the measured length of the HB, implying that the cluster is likely to possess a population of RR Lyrae stars. Our observational baseline, however, does not span a sufficiently long interval to allow a useful variability search to be performed. Overall, the morphology of the HB and the implied presence of RR Lyrae stars, together with the steep RGB, are indicative of a very old ($\gtrsim$10 Gyr) metal-poor stellar population.

For ancient systems such as this, the locus of the RGB above the level of the HB is mostly dependent on the metal abundance and only weakly sensitive to age. The observed shape of this feature therefore provides a useful and well-established probe of the cluster metallicity (e.g. Sarajedini 1994). Meanwhile, the observed level of the HB and the apparent colour of the RGB at the HB level allow estimates to be made of the distance to the cluster and the amount of foreground reddening. In order to obtain such measurements for MGC1, we compared our CMDs with fiducial sequences observed for several Galactic globular clusters in the SDSS photometric system. We subsequently checked the consistency of our results by fitting theoretical isochrones from stellar models calculated by two different groups.

### 3.2 Comparison with Galactic globular clusters

An et al. (2008) provide CMDs in the SDSS photometric system for 17 Galactic globular clusters spanning a wide range of metal abundances, $-2.3 \lesssim$ [Fe/H] $\lesssim -0.7$. Unfortunately for the purposes of estimating a photometric metallicity for MGC1, many of the CMDs they provide (and in particular those for all but one of the clusters with [Fe/H] $\lesssim -2$) are truncated only a magnitude or two above the HB level due to the saturation limits of the SDSS imagery (see their fig. 12). None the less, there are two well-populated clusters with abundances in the range of interest that are sufficiently distant for the entire extent of their RGBs to be sampled. These are

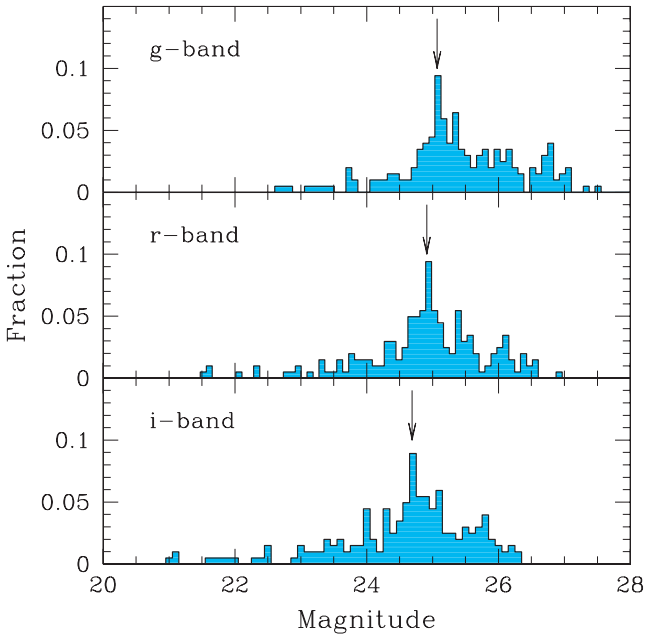


**Figure 4.** Cluster luminosity functions in each passband, constructed using only stars in the radial range 12–40 arcsec. The HB level is clearly visible and is marked with an arrow in each panel.

NGC 2419 and 7006, which have [Fe/H] = −2.12 and −1.63, respectively, according to Harris (1996).

To correctly align the fiducial sequences for these two clusters, we shifted them vertically on the CMD so that their HB levels matched that observed for MGC1, and horizontally so that their RGB colours at the level of the HB matched the observed value for MGC1. We determined the appropriate HB level for MGC1 in each of the three passbands by plotting luminosity functions. These are presented in Fig. 4 – the HB level is clearly visible in each of the histograms, at $g = 25.1, r = 24.9$ and $i = 24.7$. The uncertainty in these values is ±0.05 mag. Note that An et al. (2008) do not provide fiducial HB sequences for their clusters, however their photometry is publicly available and these ridgelines are straightforward to determine.

Because An et al. (2008) obtained their fiducial sequences from a homogeneous data set via a uniform reduction and photometry pipeline, we were able to impose an additional constraint in our alignment procedure – that the implied offsets in distance modulus ($\mu$) and foreground reddening between MGC1 and a given reference cluster should be equal on both the $(g, i)$ and $(g, r)$ CMDs. That is, for a given reference cluster we tested all likely combinations of $\Delta\mu$ and $\Delta E(B-V)$, converted these to vertical and horizontal offsets in the observational plane, and determined which combination gave the closest alignment between the observed globular cluster fiducial and MGC1 on both the $(g, i)$ and $(g, r)$ CMDs simultaneously. To convert $\Delta\mu$ and $\Delta E(B-V)$ to vertical and horizontal shifts, we used the coefficients from Stoughton et al. (2002), which relate the foreground extinction to $E(B-V)$ in SDSS passbands: $A_g = 3.793E(B-V)$, $A_r = 2.751E(B-V)$ and $A_i = 2.086E(B-V)$. Given these, it is trivial to show that $E(g-i) = 1.707E(B-V)$ and $E(g-r) = 1.042E(B-V)$.

The results for NGC 2419 and 7006 are presented in Fig. 5. The RGB fiducial for NGC 7006 is clearly much too red, implying that MGC1 is nowhere near as metal rich as this cluster. In contrast, the fiducial for NGC 2419 provides a much better fit along the majority of the RGB, only diverging marginally to the red towards the top. This suggests that MGC1 has a metal abundance close to, but still below, that of NGC 2419 at [Fe/H] = −2.12.

To explore this further, we used the observations of Clem, Vanden Berg & Stetson (2008) who provide a fiducial RGB sequence for the very metal-poor Galactic globular cluster M92 ([Fe/H] = −2.28) in the $u'\ g'\ r'\ i'\ z'$ photometric system, which is very similar (but not identical) to the instrumental SDSS *ugriz* system used here and

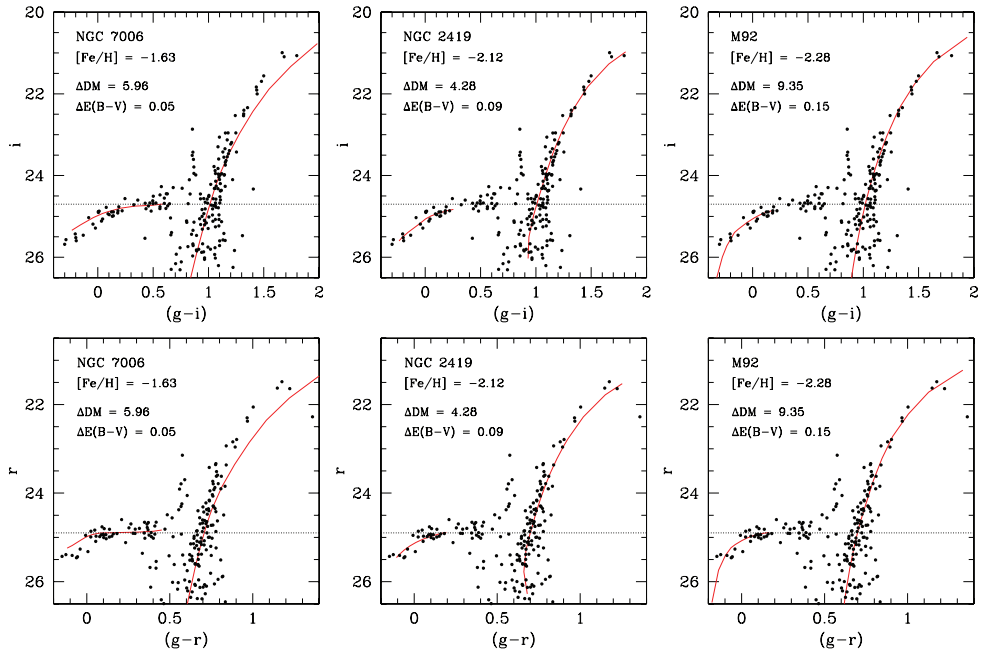


**Figure 5.** Fiducial sequences (solid lines) for the Galactic globular clusters NGC 7006 (left-hand panels), NGC 2419 (centre panels), and M92 (right-panels) overlaid on the $(g, i)$ and $(g, r)$ CMDs for MGC1. The RGB sequence for NGC 7006 ([Fe/H] = −1.63) is much too red to provide a good fit to that of MGC1. In contrast, the sequence for NGC 2419 ([Fe/H] = −2.12) provides a much better fit but diverges slightly to the red on the uppermost RGB, while the sequence for M92 ([Fe/H] = −2.28) provides an excellent fit along the full extent of the RGB.

**Table 1.** Results from fitting metal-poor Galactic globular cluster fiducials to the CMD of MGC1.

| Cluster | [Fe/H][a] | $E(B-V)^b$ | $\mu_0{}^b$ | $\Delta E(B-V)$ | $\Delta\mu$ | $E(B-V)_{\rm MGC1}$ | $\mu_{\rm MGC1}$ |
|---|---|---|---|---|---|---|---|
| NGC 2419 | −2.12 | 0.09 | 19.69 | 0.09 | 4.28 | 0.18 | 23.97 |
| NGC 5466 | −2.22 | 0.01 | 15.97 | 0.14 | 7.97 | 0.15 | 23.94 |
| M15 | −2.26 | 0.10 | 15.06 | 0.09 | 8.80 | 0.19 | 23.86 |
| M92 | −2.28 | 0.02 | 14.58 | 0.15 | 9.35 | 0.17 | 23.93 |
| NGC 5053 | −2.29 | 0.03 | 16.10 | 0.16 | 7.75 | 0.19 | 23.85 |

[a]Metal abundance as listed by Harris (1996) in the 2003 online update.
[b]Foreground reddening is calculated as the average of the values from Harris (1996) and Schlegel et al. (1998); extinction-corrected distance modulus is calculated using this value and the apparent visual distance modulus listed by Harris (1996).

by An et al. (2008). The following relations, provided by Tucker et al. (2006), allowed us to transform the Clem et al. (2008) M92 fiducial into the SDSS *ugriz* system,

$$\begin{aligned} g &= g' + 0.060\,\left[(g'-r') - 0.53\right], \\ r &= r' + 0.035\,\left[(r'-i') - 0.21\right], \\ i &= i' + 0.041\,\left[(r'-i') - 0.21\right]. \end{aligned} \quad (4)$$

An et al. (2008) demonstrate that these transformations are very accurate (better than 2 per cent) for M92 and other Galactic globular clusters. Unfortunately, Clem et al. (2008) do not provide HB fiducials for their clusters or a public archive of their photometry. Therefore, we had to use the HB fiducial for M92 that we derived from the An et al. (2008) photometry – this is evidently not ideal, but the demonstrated accuracy of the transformations listed in equation (4) means that any systematic uncertainties introduced should be, at most, a few hundredths of a magnitude.

The results we obtained by aligning these M92 fiducials are also presented in Fig. 5. On both the $(g, i)$ and $(g, r)$ CMDs, the agreement is very close along the full length of the RGB for identical distance modulus and foreground reddening. It thus seems likely that MGC1 has a very low metal abundance, with [Fe/H] $\approx -2.3$. It is worth noting that this value is more metal poor than the initial estimate by Martin et al. (2006), who obtained [Fe/H] $\sim -1.3$, and also the value of [Fe/H] $\sim -1.37 \pm 0.15$ measured from high-resolution spectroscopy by Alves-Brito et al. (2009). It is, however, in good agreement with the measurement obtained spectroscopically by Galleti et al. (2007), [Fe/H] $\sim -2.1$.

In Section 2.2, we noted the lack of colour terms in our photometric calibration. It is important to assess what impact this may have on the shape of the RGB and hence on our derived metal abundance. On the $(g, i)$ CMD the part of the cluster RGB above the HB spans the colour range $1.0 \lesssim (g-i) \lesssim 1.7$. According to equation (3), the expected systematic offsets due to the omission of colour terms span the range $0.0 \lesssim \Delta(g-i) \lesssim 0.01$ over this colour interval. Similarly, the expected systematic offsets on the $(g, r)$ CMD span the range $0.01 \lesssim \Delta(g-r) \lesssim 0.02$. In both cases, the result of adding colour terms is to stretch the RGB to the red, making it appear more metal-rich than in the present CMDs. However, the expected magnitude of this effect is too small to significantly alter our derived metal abundance.

The horizontal and vertical shifts required to align the M92 fiducials with our CMDs allow us to estimate the foreground reddening and distance modulus for MGC1. Both Harris (1996) and Schlegel, Finkbeiner & Davis (1998) agree that $E(B-V) = 0.02$ for M92, resulting in an extinction-corrected distance modulus of $\mu = 14.58$ for this cluster (Harris 1996). The horizontal and vertical offsets we derived, as noted in Fig. 5, then imply that the foreground reddening towards MGC1 is $E(B-V) = 0.17$, and the distance modulus for this cluster is $\mu = 23.93$.

There are three additional Galactic globular clusters in the sample of An et al. (2008) that have metal abundances comparable to that of M92: M15, NGC 5053 and NGC 5466. All these have truncated RGB sequences and are hence not useful for obtaining a precise metallicity estimate for MGC1, however their observed fiducials are none the less suitable for determining additional estimates of the foreground reddening and distance modulus of MGC1, on the basis that they are all sufficiently similar in metal abundance for our alignment procedure to provide physically meaningful results.

Table 1 summarizes the values of distance modulus and foreground extinction derived from fitting these cluster fiducials to our CMDs; we have also included NGC 2419 for comparison. Random uncertainties in individual values of $\mu$ and $E(B-V)$ are related to the errors associated with aligning the fiducials correctly. Experimentation shows that fiducials shifted by $\pm 0.02$ mag in colour and in the range $\pm 0.05-0.1$ mag in brightness result in notably poorer fits. The relationships between $E(B-V)$, and $E(g-i)$ and $E(g-r)$ mean that the random uncertainties in $E(B-V)$ are then better than 0.02 mag. The contribution to the uncertainty in $\mu$ from the vertical alignment precision is therefore dominant over the contribution from the uncertainty in the calculated extinction, and we hence assume the random uncertainty in distance modulus to be $\pm 0.1$ mag. We note that there is also a systematic contribution due to the uncertainty in our estimation of the correct HB levels – Fig. 4 suggests this is of order $\pm 0.05$ mag at most.

Our derived colour excesses and distance moduli for MGC1 both exhibit small dispersions across the sample of comparison clusters. The rms values are $E(B-V) = 0.18 \pm 0.02$ and $\mu = 23.91 \pm 0.06$. We discuss these results and their implications in more detail in Section 3.4.

### 3.3 Comparison with theoretical isochrones

To check the consistency of our results, including their robustness to variations in both the assumed age and $\alpha$-element enhancement of MGC1 (neither of which are tightly constrained by observation), we employed theoretical isochrones calculated by two different groups. We downloaded models of both scaled-solar and $\alpha$-enhanced composition – Galactic globular clusters typically exhibit enhancement in $\alpha$-elements compared to the solar abundance, of roughly $[\alpha/{\rm Fe}] \sim +0.3$ (see e.g. Carney 1996). We initially selected models as close as possible to ∼12.5 Gyr old (taken to be representative of the age of the oldest metal-poor Galactic globular clusters), but subsequently tested how our results varied with changes in age of $\pm 2$ Gyr either side of this value. In more detail, we used the following.

(i) BaSTI models (Pietrinferni et al. 2004, 2006), for which we downloaded isochrones of age 12.5 Gyr, scaled-solar composition, and metal abundances of [Fe/H] = −1.79 and −2.27; along with isochrones again of age 12.5 Gyr, $\alpha$-enhanced composition with [$\alpha$/Fe] = +0.4, and iron abundances of [Fe/H] = −2.14 and −2.62.

(ii) Dartmouth models (Dotter et al. 2007, 2008), for which we downloaded isochrones of age 12.7 Gyr, metal abundances sampling the range $-2.5 \leq$ [Fe/H] $\leq -1.6$ at 0.3 dex intervals, canonical Helium abundance ($Y \approx 0.245$), and both scaled-solar and $\alpha$-enhanced composition – the latter with [$\alpha$/Fe] = +0.4. Unlike the BaSTI isochrones which include post-RGB evolution, the Dartmouth group provides separate synthetic HB models.

Although models by the Padova group (Girardi et al. 2000, 2004; Marigo et al. 2008) are also commonly employed, we elected not to use these in the present work for two reasons. First, Padova models with $\alpha$-enhanced composition are not presently available for the suspected age and metallicity of MGC1. Secondly, it is known that the scaled-solar Padova models in the SDSS *ugriz* system for ancient metal-poor systems generally possess redder RGB loci than should be expected. A particular example of this may be seen in Girardi et al. (2004) where Padova isochrones in the SDSS photometric system with [Fe/H] = −1.7 provide a good fit to the RGB of the Galactic globular cluster NGC 2419, which is ≈0.4 dex more metal-poor than this.

We overlaid the isochrones using the same methodology as that described in Section 3.2 – shifting them vertically on the CMD so that their HB levels matched that observed for MGC1, and horizontally so that their RGB colours at the level of the HB matched the observed value. In this case, however, since we were dealing with theoretical isochrones (which represent the output of stellar evolution models transformed on to the observational plane), we were forced to relax the additional constraint that the implied distance modulus and foreground extinction be identical for both the ($g$, $i$) and ($g$, $r$) CMDs.

Fig. 6 shows aligned scaled-solar isochrones with a variety of metallicities on our ($g$, $i$) and ($g$, $r$) CMDs. The results are in excellent agreement with the metallicity estimate of [Fe/H] ≈ −2.3 that we obtained by aligning Galactic globular cluster fiducials on the CMD. Here, the BaSTI isochrone with [Fe/H] = −2.27 fits the cluster RGB most closely, whereas the next available isochrone with [Fe/H] = −1.79 is clearly too metal rich. Similarly, the Dartmouth isochrones with [Fe/H] = −2.5 and [Fe/H] = −2.2 both provide reasonably good matches to the observed RGB, while the isochrone with [Fe/H] = −1.9 is clearly too metal rich. From these models, we therefore infer [Fe/H] ≈ −2.35. To confirm that such measurements are not sensitive to the selected age, we repeated the alignment procedure using sets of 10 and 15 Gyr old isochrones, obtaining consistent results to within ≈0.15 dex.

Fig. 7 shows aligned $\alpha$-enhanced isochrones on our ($g$, $i$) and ($g$, $r$) CMDs. The degree of $\alpha$-enhancement is marginally higher than the [$\alpha$/Fe] ∼ +0.3 typically observed for Galactic globular clusters and thus likely represents the maximum effect $\alpha$-enhancement in MGC1 would have on the metallicity estimates we obtained from scaled-solar models. The two $\alpha$-enhanced BaSTI isochrones correspond to total metallicities of [M/H] = −2.27 and −1.79 (Pietrinferni et al. 2006), and therefore have lower iron abundances than the scaled-solar models in Fig. 6. The three $\alpha$-enhanced Dartmouth models, on the other hand, have the same iron abundances as the previous scaled-solar models and therefore higher total metallicities.

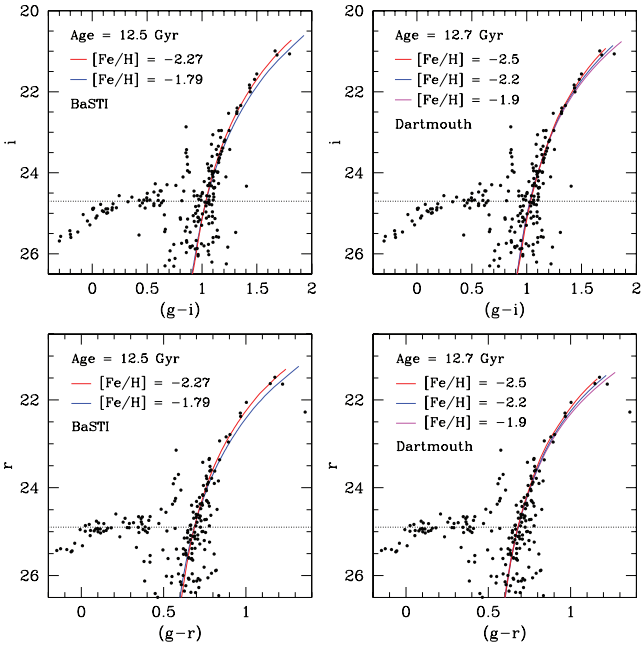


**Figure 6.** RGBs from scaled-solar isochrones calculated by the BaSTI and Dartmouth groups overlaid on our cluster ($g$, $i$) and ($g$, $r$) CMDs. In each panel, the isochrone with the best-fitting metallicity is plotted with a thick red line. The black dotted lines mark the adopted cluster HB level, from Fig. 4.

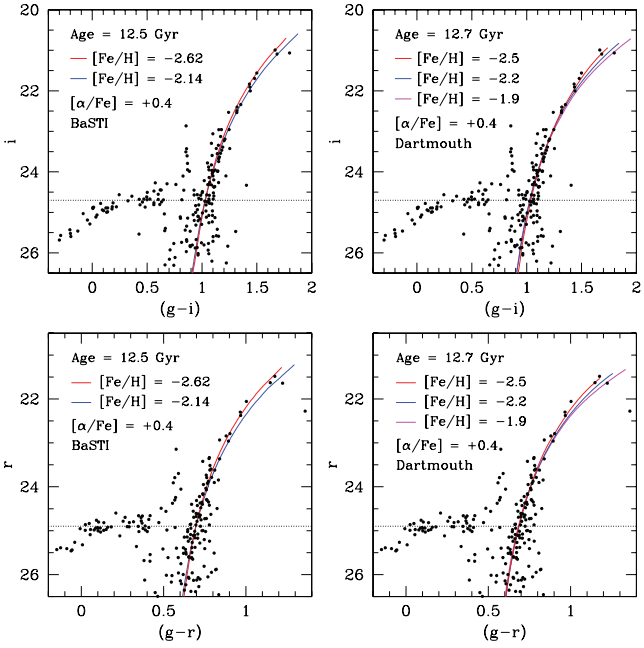


**Figure 7.** Same as Fig. 6, but for $\alpha$-enhanced isochrones with [$\alpha$/Fe] = +0.4 from the BaSTI and Dartmouth groups.

Adopting the relation of Salaris, Chieffi & Straniero (1993),

$$[\mathrm{M/H}] = [\mathrm{Fe/H}] + \log(0.638\, f_\alpha + 0.362), \quad (5)$$

where $f_\alpha = 10^{[\alpha/\mathrm{Fe}]}$ is the $\alpha$-element content, these isochrones correspond to total metallicities of [M/H] ≈ − 2.2, −1.9 and −1.6, respectively. From Fig. 7, it is clear that for both the BaSTI and Dartmouth models it is the most metal poor isochrone that provides the best fit to the cluster RGB, implying that if MGC1 has an

**Table 2.** Results from fitting theoretical isochrones to the CMD of MGC1.

| Isochrone Set | Filters | [Fe/H] | [$\alpha$/Fe] | [M/H] | $\mu$ | $E(B-V)$ |
|---|---|---|---|---|---|---|
| BaSTI | $(g,i)$ | −2.27 | 0.0 | −2.27 | 23.97 | 0.18 |
| BaSTI | $(g,i)$ | −2.62 | +0.4 | −2.27 | 23.93 | 0.19 |
| BaSTI | $(g,r)$ | −2.27 | 0.0 | −2.27 | 24.10 | 0.15 |
| BaSTI | $(g,r)$ | −2.62 | +0.4 | −2.27 | 24.03 | 0.17 |
| Dartmouth | $(g,i)$ | −2.35 | 0.0 | −2.35 | 23.95 | 0.18 |
| Dartmouth | $(g,i)$ | −2.50 | +0.4 | −2.21 | 24.01 | 0.18 |
| Dartmouth | $(g,r)$ | −2.35 | 0.0 | −2.35 | 24.00 | 0.16 |
| Dartmouth | $(g,r)$ | −2.50 | +0.4 | −2.21 | 24.08 | 0.15 |

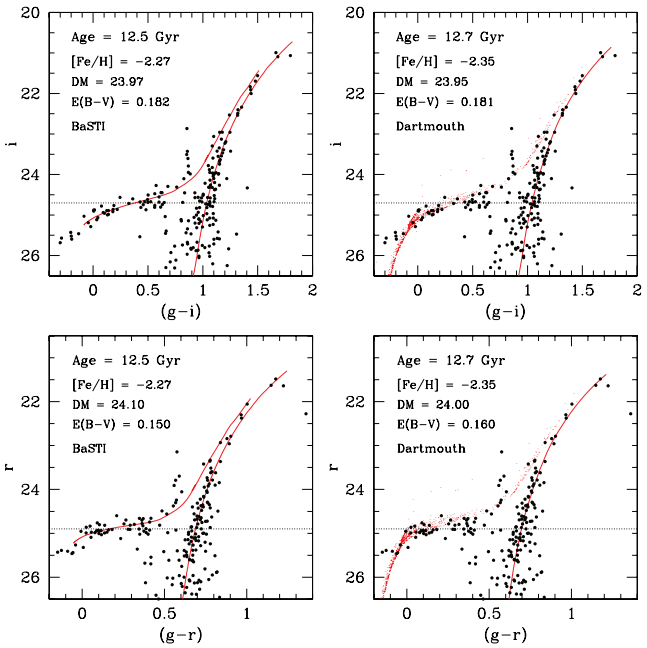


**Figure 8.** CMDs showing the complete best-fitting scaled-solar isochrones from the BaSTI and Dartmouth groups. The values of $\mu$ and $E(B-V)$ required to align a given isochrone are listed in each panel and summarized in Table 2.

$\alpha$-enhanced rather than solar-like composition it is still a very metal poor object with [M/H] $\approx -2.2$ or $-2.3$. Once again, this is in excellent agreement with the metallicity estimate that we obtained by aligning Galactic globular cluster fiducials.

For each set of isochrones, we again used the offsets required to align the best-fitting model with the CMD to determine estimates of the MGC1 distance modulus and foreground extinction. Our results are presented in Table 2, while Fig. 8 shows examples of the aligned best-fitting scaled-solar isochrones from both group. As previously, random uncertainties in the derived distance moduli and colour excesses are related to the errors associated with aligning the isochrones correctly, and we assume these to be better than 0.02 mag in $E(B-V)$ and $\pm 0.1$ mag in $\mu$.

The derived values of distance modulus and foreground reddening listed in Table 2 show good consistency irrespective of the adopted isochrone set or $\alpha$-element abundance. More specifically, the calculated distance moduli span the range 23.93–24.10 with an rms value of $\mu = 24.00 \pm 0.06$, while the $E(B-V)$ measurements span the range $0.15 - 0.19$ with an rms value of $0.17 \pm 0.02$. These results are entirely consistent with those we derived by fitting Galactic globular cluster fiducials to our CMDs.

### 3.4 MGC1 distance and foreground extinction

Overall, our best estimate for the distance modulus of MGC1 is $23.91 \pm 0.06$ from fitting Galactic globular cluster fiducials to our CMD, and $24.00 \pm 0.06$ from fitting theoretical isochrones. These correspond to line-of-sight distances of 605 and 630 kpc, respectively, indicating that MGC1 lies substantially nearer to us than do the central regions of M31, which have a line-of-sight distance of $\approx$780 kpc ($\mu_{\rm M31} = 24.47 \pm 0.07$; McConnachie et al. 2005). This result is consistent with the previous distance estimated for MGC1 by Martin et al. (2006).

The distance we have measured for MGC1 allows us to estimate the three-dimensional (deprojected) distance between this cluster and the centre of M31. In doing so, we adopt $\mu_{\rm M31} = 24.47 \pm 0.07$ along with a corresponding projected distance between the cluster and M31 of $R_{\rm p} = 117$ kpc. The derived deprojected galactocentric radius of MGC1 is then 205 kpc for a distance modulus of 23.91 and $R_{\rm gc} = 185$ kpc for $\mu = 24.00$. Recalling that the $1\sigma$ uncertainties on our measured distance moduli are $\pm 0.06$ mag, the uncertainties in these deprojected radii are $\pm 20$ kpc.

Meanwhile, our estimate of the MGC1 colour excess is $E(B-V) = 0.18 \pm 0.02$ from fitting Galactic globular cluster fiducials to our CMD, and $E(B-V) = 0.17 \pm 0.02$ from fitting theoretical isochrones. These values are a factor of two larger than the prediction from the reddening maps of Schlegel et al. (1998) for this region of the sky: $E(B-V) = 0.086$. Because this discrepancy exists for all of the different Galactic globular cluster fiducials we considered, for all of the different isochrone sets we used, and because it occurs consistently on both the $(g,r)$ and $(g,i)$ CMDs, it is unlikely to be a result of our data reduction or analysis. It cannot also be due to the omission of colour terms in determining our photometric calibrations, as we discuss below.

A possible explanation for our large inferred $E(B-V)$ value may be seen from examination of wide-field imaging of the region surrounding the cluster. Fig. 9 shows a $6 \times 6$ arcmin$^2$ $g$-band image centred on the cluster, excised from Subaru Suprime-Cam observations targeting the dwarf galaxy And XIII (Martin et al., in preparation) which lies projected nearby to MGC1. The image shows nebulosity varying across the region, implying that there is variable extinction present on scales much smaller than the $6 \times 6$ arcmin$^2$ resolution of the Schlegel et al. (1998) maps. In particular, inspection of Fig. 9 reveals that the excess nebulosity happens to be large on the cluster, consistent with our derived colour excess. We note that a similar pattern is also visible on the MegaCam survey imaging of this region from which MGC1 was discovered, and also, to some extent, on our GMOS imaging. This consistency indicates that the nebulosity visible in Fig. 9 is a real feature of this part of the sky, and not simply due to a flat-fielding error or to scattered light on the Subaru image.

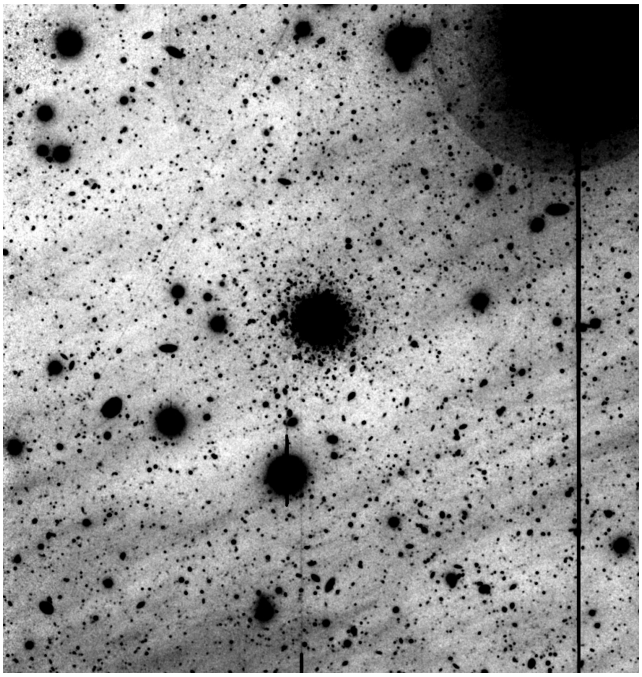

**Figure 9.** Subaru/Suprime-Cam $g$-band cut-out of MGC1, spanning 6 × 6 arcmin$^2$, showing the spatially variable nebulosity found in this part of the sky. The image has been smoothed slightly with a Gaussian kernel of FWHM ∼2 pixels (≈0.4 arcsec) and then had an appropriate linear scaling applied to show the local excess nebulosity clearly. North is towards the top of the image and east is to the left.

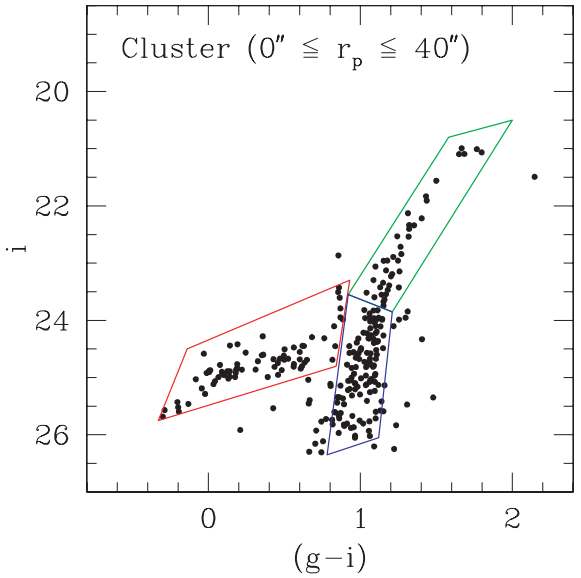


**Figure 10.** All detected stars within 40 arcsec of the centre of MGC1 plotted on a $(g, i)$ CMD. These sequences define the three selection boxes (marked) that we used to identify probable cluster members at larger radii.

It is worthwhile considering the effects that the omission of colour terms from our photometric calibration (see Section 2.2) might have on our derived distance modulus and foreground extinction. These quantities were measured by registering fiducial sequences to the cluster HB luminosity and RGB colour. On the $(g, i)$ CMD, the level region of the HB occurs at $(g - i) \approx 0.5$. Equation (3) then suggests that leaving out colour terms in our photometric calibration results in an $i$-band HB magnitude that is too faint by ∼0.01 mag. In other words, incorporating this correction would make the distance modulus shorter by ∼0.01 mag. Similarly, the colour of the RGB at the HB level is $(g - i) \approx 1.0$. Again using equation (3), at this colour the effect of omitting colour terms from our photometric calibration is negligible, $\Delta(g - i) \approx 0.00$. For the RGB above the HB level, the effect of omitting colour terms is to produce an RGB that is too blue by up to ∼0.01 mag. Thus, including the colour terms would only act to increase our derived colour excess. Following the same process for the $(g, r)$ CMD, we obtain very similar results. Overall, it is then clear that (i) including colour terms in our photometric calibration would not have resulted in our deriving a larger distance modulus or smaller foreground extinction for MGC1 and (ii) the expected corrections are, in any case, negligible in size.

## 4 CLUSTER STRUCTURE AND LUMINOSITY

We determined the radial density profile of MGC1 in each of our three photometric passbands via a combination of surface photometry in its unresolved central regions, and star counts at larger radii. We obtained surface photometry by using the PHOT task in IRAF to measure the flux through circular apertures of increasing size, and then converting these into measurements of the surface brightness in concentric circular annuli. An estimate of the sky background was determined from several blank regions near the cluster, and subtracted from each annulus. We desired to extend the integrated-light photometry as far from the cluster centre as possible to maximize overlap with star-count profiles (see below); in practice we were limited to a maximum radius $r_p = 35$ arcsec, beyond which the flux contribution from objects not belonging to the cluster became non-negligible (as determined from the CMD). Even within this radius, there were several significant background galaxies evident on the images (see Fig. 1); these were masked prior to our measurements. The surface photometry was transformed on to the SDSS photometric system via equation (2).

We employed star counts to extend the radial profile beyond 35 arcsec. To minimize the contamination from non-cluster members, we only counted stars falling in several empirically determined regions on both the $(g, i)$ and $(g, r)$ CMDs. On each CMD, we used stellar detections within 40 arcsec of the centre of MGC1 to define three boxes preferentially inhabited by cluster members – one region enclosing the HB, and one each for the lower and upper RGB. Because we suspected variable foreground extinction on scales of a few arcmin or less (see Section 3.4), we ensured these CMD regions were sufficiently broad to accommodate changes in $E(B - V)$ of up to ±0.1 mag away from the cluster centre. Example selection boxes for the $(g, i)$ CMD can be seen in Fig. 10.

Our star-count annuli extended from the innermost regions of MGC1 out to the edges of our stacked images at $r_p = 150$ arcsec. To ensure consistency with the inner surface photometry, in each individual annulus we converted the summed flux of the counted stars into a surface brightness. Because this process did not include unresolved diffuse cluster light, there was a clear offset between our star-count profile and that from the inner surface photometry. To join the two profiles, we considered an overlap region, extending inwards from 35 arcsec to a radius where we judged that incompleteness due to crowding was having a significant effect on the star-count profile. This was clearly visible as a point near $r_p \approx 13$ arcsec where the shapes of the two profiles began to diverge – that from the star counts flattening and falling below that from the surface photometry.

Although our CMD selection boxes greatly reduced contributions to the star-count profile from non-cluster objects, there was still

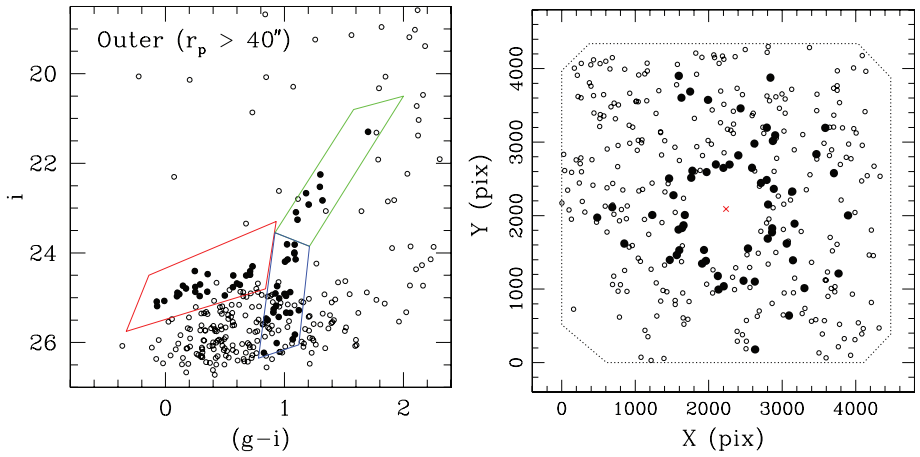


**Figure 11.** All stellar objects in our GMOS field outwith 40 arcsec from the centre of MGC1. Left-hand panel: plotted on a $(g, i)$ CMD along with the selection boxes from Fig. 10. Right-hand panel: spatial positions on the GMOS field of view. In each panel, stars which fell within selection boxes on both the $(g, i)$ and $(g, r)$ CMDs are marked with solid black circles; all other stellar objects are marked with open circles. In the left-hand panel, there are clear overdensities of stars visible at the blue end of the HB and halfway up the RGB, indicating the presence of cluster members at large radii. The right-hand panel shows that these members extend to the edge of the field of view (marked with dotted lines) and appear to be fairly evenly distributed about the cluster centre (marked with a cross).

undoubtably sufficient contamination that it was necessary for us to correct for this. We originally planned to use the outermost regions of our GMOS imaging to define the background level, however, to our surprise, the star-count profile was still clearly falling steeply as a function of radius to the very edges of the field – indicative of a significant contribution from cluster members even at large radii. Evidence of this may be seen in Fig. 11, the left-hand panel of which shows a CMD for all stellar objects at radii beyond 40 arcsec. Objects falling in the selection boxes on both the $(g, i)$ and $(g, r)$ CMDs are marked with large solid circles. Although there is certainly contamination in the $(g, i)$ CMD selection boxes from non-cluster members, there is also a significant number of stars falling very close to where the main cluster sequences are expected. In particular, a clear overdensity of stars is visible at the blue end of the HB, as well as around the join between the lower and upper RGB. Many of these objects fall at radii even beyond 80 arcsec. A plot of their spatial positions (right-hand panel of Fig. 11) reveals them to be fairly evenly distributed about the cluster – no striking azimuthal asymmetry is evident.

To obtain an estimate of the background level and trace the outermost regions of the cluster profile, we utilized two supplementary wide-field data sets – photometry from the CFHT/MegaCam survey imaging in which MGC1 was discovered (see Martin et al. 2006; Ibata et al. 2007), and photometry from the Subaru Suprime-Cam observations noted in Section 3.4 (see Martin et al., in preparation). The CFHT observations are in the MegaCam $g$ and $i$ passbands[3] and are roughly 1.5–2 mag shallower than our GMOS observations. The Subaru observations are intermediate in both depth and image quality between our GMOS observations and the CFHT imaging. Both the Subaru/Suprime-Cam and CFHT/MegaCam photometric data sets were obtained as end-products from versions of the Cambridge Astronomical Survey Unit reduction pipeline (Irwin & Lewis 2001). Both cover regions of sky to radii at least ∼2000 arcsec from the centre of MGC1.

To utilize these data sets, we followed a similar procedure to that for constructing our GMOS star-count profile. We first defined appropriate selection boxes on the respective $(g, i)$ CMDs by using stars within 40 arcsec of the cluster centre, although we were careful to (i) exclude the most crowded inner regions in both sets where the photometry is degraded and (ii) not include objects too close to the faint limit in the Subaru photometry, which is spatially variable over the full field of view. We then used these selection boxes to perform star counts in concentric circular annuli extending to 400 arcsec from the cluster centre. We determined the background level by considering a wide annulus exterior to this, spanning $r_p$ = 400–2000 arcsec. We joined the two profiles to our composite GMOS profile by considering the overlap in the radial range 20–150 arcsec. Note that the MegaCam photometry is not strictly on the same system as the GMOS and Subaru photometry, however, assuming there is no strong colour gradient in the outer regions of the MGC1 profile, the difference is, to a good approximation, a small constant offset in magnitude.[4]

The final $g$-band background-subtracted radial brightness profile for MGC1 may be seen in Fig. 12. The background levels measured from the MegaCam and Subaru photometry agree to within 0.1 mag and are marked by the horizontal dotted lines. We determined uncertainties in the central surface photometry by splitting a given annulus into up to eight segments and considering the variance in flux between them. The resulting error-bars are smaller than the sizes of the plotted points. Uncertainties in the star count profiles were calculated using a combination of Poisson statistics and the uncertainty in the background subtraction. To avoid congestion in the figure, we have marked errorbars on the Subaru annuli only, however, these are indicative of the typical uncertainty at a given radius. The vertical dashed line marks the FWHM of the GMOS $g$-band PSF, and is thus the approximate radius interior to which atmospheric seeing strongly affects the cluster profile.

The GMOS measurements alone (solid black circles and magenta triangles) show that the cluster can be reliably traced to a radius $r_p$ = 150 arcsec ≈450 pc (assuming $\mu$ = 23.95), at which point the surface brightness is comparable to the background contribution. Points exterior to this are strongly sensitive to the adopted

[3] Which are similar, but not identical, to the SDSS $g$ and $i$ filters.

[4] http://www2.cadc-ccda.hia-iha.nrc-cnrc.gc.ca/megapipe/docs/filters.html

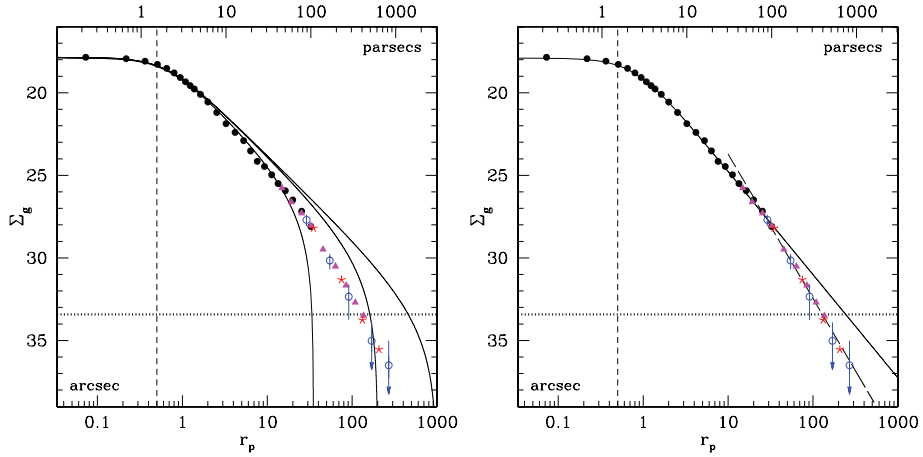


**Figure 12.** Radial background-subtracted SDSS $g$-band surface brightness profile for MGC1. The solid black circles indicate integrated-light photometry in the unresolved central regions from our GMOS imaging, while the solid magenta triangles denote star-count measurements at larger radii from the same observations. At larger radii still, star counts from our CFHT/MegaCam survey imaging are indicated by red stars, while star counts from Subaru/Suprime-Cam are marked by open blue circles. Uncertainties are plotted on the Subaru points; at given radius these are typical for all the star-count measurements. Background levels derived from the MegaCam and Suprime-Cam observations are marked with horizontal dotted lines; these agree to better than 0.1 mag. The vertical dashed line indicates the 0.5 arcsec FWHM of the $g$-band PSF; at smaller radii atmospheric seeing strongly affects the profile. The left-hand panel shows three King (1962) models with $r_c = 0.65$ arcsec and $r_t = 35$, 200 and 1000 arcsec. The right-hand panel shows our best-fitting EFF model, which has $a = 0.8$ arcsec and power-law fall-off $\gamma = -2.5$. There is a break to a steeper power-law fall-off with $\gamma = -3.5$ (long-dashed line) around $r_p \sim 35$ arcsec.

background level, but, taken at face value, the profile apparently extends to ∼250–300 arcsec ≈750–900 pc without showing a clear tidal cut-off.

We attempted to fit, by $\chi^2$ minimization, two sets of commonly used models to the MGC1 profile. The first was empirical King (1962) models of the form:

$$\Sigma(r_p) = \Sigma_0 \left[ \frac{1}{\sqrt{1+(r_p/r_c)^2}} - \frac{1}{\sqrt{1+(r_t/r_c)^2}} \right]^2, \quad (6)$$

where $r_t$ is the tidal cut-off radius, $r_c$ is the core radius and $\Sigma_0$ is a scaling parameter. As long as one is not dealing with a low-concentration cluster (i.e., provided $r_t \gg r_c$), $\Sigma_0$ is approximately equal to the central surface brightness, and $r_c$ is roughly the radius where the surface brightness has fallen to half of its central value.

We also fit models of the form described by Elson, Fall & Freeman (1987, hereafter EFF),

$$\Sigma(r_p) = \Sigma_0 \left(1 + \frac{r_p^2}{a^2}\right)^{-\gamma/2}, \quad (7)$$

which are similar to the King (1962) models in their central regions but have no outer tidal cut-off, instead approaching a power-law fall-off with exponent $-\gamma$ at large radius. Here, the scale radius $a$ is related to the King core radius $r_c$ by

$$r_c = a\sqrt{2^{2/\gamma} - 1} \quad (8)$$

provided, once again, that $r_t \gg r_c$.

The results of our model fitting are displayed in Fig. 12. The left-hand panel shows that while a King profile fits the inner regions of MGC1 well, in the outer parts these models do not provide a good description of the observed shape of the profile, even if a wide variety of tidal radii are invoked (the three examples plotted have $r_c = 0.65$ arcsec and $r_t = 35$, 200 and 1000 arcsec). The EFF family of models does somewhat better, although a single set of parameters cannot describe the full radial extent of the observations. The cluster apparently closely follows a power-law fall-off in its outer regions, but there is a break around $r_p \sim 35$ arcsec from a profile with exponent $\gamma \approx -2.5$ to a steeper fall-off with $\gamma \approx -3.5$. It is notable that the break occurs roughly where our composite profile transitions from surface photometry to star counts, and a stellar luminosity function that steepens with radius could thus potentially be responsible. However, the fact that the break can apparently be seen when considering only the GMOS star counts alone (magenta triangles) argues against this interpretation.

Our best-fitting models allow us to precisely estimate the cluster core radius: the King profiles have $r_c = 0.65$ arcsec ≈2.0 pc, while the EFF model has $a = 0.80$ arcsec which corresponds to $r_c = 0.69$ arcsec ≈2.1 pc (assuming $\gamma = -2.5$, which is most appropriate for the inner part of the observed profile). Both sets of models converge to a central surface brightness $\Sigma_g(0) = 17.85$ mag arcsec$^{-2}$. Our measured values for $r_c$ are close to the FWHM of the PSF for the $g$-band observations, and could therefore conceivably be smaller than we have measured here. Such a scenario would also result in a larger central surface brightness than we have determined. Higher resolution observations of MGC1 will be required to test this possibility. For now, we simply note that many globular clusters with smaller $r_c$ and higher central surface brightness than we have measured for MGC1 are known in both the inner and outer regions of M31 (e.g. Barmby, Holland & Huchra 2002; Tanvir et al. 2009).

Our observed profile also allows an estimation of the cluster luminosity. Integrating the measured surface brightness out to the edge of the GMOS field at $r_p = 150$ arcsec, and subtracting the Subaru/MegaCam background level results in a total apparent luminosity $m_g = 15.74$.[5] Assuming $\mu = 23.95 \pm 0.06$ and $E(B-V) = 0.18 \pm 0.02$ leads to an absolute $g$-band magnitude $M_g = -8.9 \pm 0.2$. We can convert this to a standard $V$-band magnitude by

[5] It is unnecessary to integrate to larger radii, where the background-subtracted profile is quite uncertain, as this adds at most a few hundredths of a magnitude to the total luminosity.

**Table 3.** Structural and luminosity measurements for MGC1.

| Parameter | Value[a] |
|---|---|
| $\Sigma_g(0)$, $\Sigma_r(0)$, $\Sigma_i(0)$ | $17.85^m$, $17.17^m$, $16.83^m$ |
| $\Sigma_{V,0}(0)$ | $16.95^m$ |
| $r_c$ (King) | 0.65 arcsec (≈2.0 pc) |
| $r_t$ (King) | Indeterminate |
| $r_c$ (EFF) | 0.69 arcsec (≈2.1 pc) |
| $\gamma$ (EFF) | $-2.5 \rightarrow -3.5$ |
| $r_h$ | 2.5 arcsec (≈7.5 pc) |
| $m_g$ | $15.74^m$ |
| $M_g$ | $-8.9^m$ |
| $M_V$ | $-9.2^m$ |
| $L_{tot}$ | $4.05 \times 10^5\ L_\odot$ |
| $(g-r)$, $(g-i)$ | $0.64^m$, $1.03^m$ |
| $(V-I)_0$ | $0.89^m$ |

[a]A distance modulus of $\mu = 23.95$ and foreground extinction $E(B-V) = 0.18$ have been used where appropriate.

adopting $M_{V,\odot} = +4.82$ and $M_{g,\odot} = +5.12$ (see the SDSS DR7 website as specified in Section 2.2). This results in $M_V = -9.2 \pm 0.2$, rendering MGC1 a rather luminous globular cluster with $L_{tot} \approx 4.05 \times 10^5\ L_\odot$. Our result is significantly more luminous than the value derived by Martin et al. (2006), however, the difference can be entirely attributed to our larger assumed foreground extinction, as well as the fact that we have traced the cluster profile to a much larger radius.

Repeating this exercise for the $r$ and $i$ bands leads to apparent integrated colours of $(g-r) = 0.64$ and $(g-i) = 1.03$. Correcting for foreground extinction and transforming to standard magnitudes using the relations on the SDSS DR7 webpage results in $(V-I)_0 = 0.89$ for MGC1, which is completely consistent with the integrated colours of other remote globular clusters in both M31 (e.g. Huxor et al. 2009) and the Milky Way (e.g. Harris 1996).

Finally, returning to our $g$-band profile it is straightforward to determine the half-light radius $r_h = 2.5$ arcsec ≈7.5 pc. This is larger than the value of $2.3 \pm 0.2$ pc measured by Martin et al. (2006), however, much of this discrepancy is due to our larger measured integrated luminosity – adopting that determined by Martin et al. (2006) yields an $r_h$ smaller by at least a factor of 2. A summary of our structural and luminosity measurements for MGC1 is provided in Table 3.

## 5 DISCUSSION

The measurements we present above suggest that MGC1 lies at a distance of $200 \pm 20$ kpc from the centre of M31. This renders it by far the most isolated globular cluster known in the Local Group – it resides at a much greater galactocentric radius than do the most remote globular clusters in the Milky Way (Palomar 4 at $R_{gc} \sim 110$ kpc and AM 1 at $R_{gc} \sim 120$ kpc) and the next most distant globular clusters known in M31 (e.g., GC10/H27 at $R_p \sim 100$ kpc; Mackey et al. 2007; Huxor et al. 2008). Indeed, our derived galactocentric radius for MGC1 is likely to represent a significant fraction of the virial radius of M31. Even so, the cluster's radial velocity of $\sim -50$ km s$^{-1}$ relative to M31 is consistent with that expected for a halo member at its observed galactocentric radius, and lies within the probable M31 escape velocity (see e.g. fig. 4 in Chapman et al. 2007). There is no implication, therefore, that MGC1 is anything so exotic as an unbound or intergalactic globular cluster. Instead, our observations suggest that the globular cluster populations of large spiral galaxies may be considerably more spatially extended than has previously been appreciated.

In this regard, it is interesting that although distinct substructures have been identified in the M31 halo to projected radii beyond 100 kpc (e.g. Ibata et al. 2007; McConnachie et al. 2009), MGC1 does not lie near any known tidal stream or halo overdensity. Rather, it falls within an area that is apparently completely free of such structures – indeed, it is the region that Ibata et al. (2007) use to define their 'clean' M31 outer halo stellar selection. It is also worthwhile noting that while MGC1 lies within a $\sim 2 \times 2$ deg$^2$ area that contains three satellite dwarf galaxies of M31 (And XI, XII and XIII), there is no evidence that any of these four objects is associated with any other. On the contrary, the three dwarfs apparently lie much closer to the M31 distance than does MGC1 (Martin et al. 2006; Martin et al., in preparation), while all four exhibit quite disparate radial velocities (see e.g. Chapman et al. 2007).

Our measurements have also shown that MGC1 is a very luminous globular cluster. Indeed, with $M_V \approx -9.2$ it would fit comfortably within the top 10 most luminous globular clusters in the Milky Way. The fact that it also lies at a very large galactocentric radius reinforces the idea, first put forward by Mackey et al. (2007) (see also Galleti et al. 2007; Huxor et al. 2009), that M31 possesses a population of very remote, compact, luminous globular clusters not seen in the Milky Way. A total of seven globular clusters are known in the very outer reaches of the Galactic halo, beyond $R_{gc} = 40$ kpc. Of these, six are subluminous (with $-6.0 \lesssim M_V \lesssim -4.7$) and rather diffuse ($11 \lesssim r_h \lesssim 25$ pc). The seventh cluster is NGC 2419, which is one of the most luminous in the Galactic system and which has a number of unusual properties that has led to suggestions that it may be the remains of an accreted galaxy (e.g. van den Bergh & Mackey 2004). In contrast, a search of the RBC reveals 34 confirmed clusters in M31 with $R_p \geq 40 \times (\pi/4) = 31.4$ kpc,[6] of which 25 are compact and nine are of the extended type first reported by Huxor et al. (2005). Assuming $\mu_{M31} = 24.47$ and a typical $E(B-V) \approx 0.1$, 12 of the 25 remote compact clusters (including MGC1) have luminosities brighter than $M_V = -8.0$, while another five have luminosities lying between this value and the peak of the GCLF at $M_V \approx -7.5$.

Given that all but three of the 34 remote M31 clusters come from the survey area described in Huxor et al. (2008), covering one quadrant of the M31 halo, this clear disparity between the remote M31 and Milky Way globular cluster systems cannot be simply due to the global difference in population size (which would account for, at most, a factor of ∼3). The origin of the differences between the Galactic and M31 outer halo globular clusters is not known. We speculate that it may be related to the apparently more vigorous accretion and merger history that M31 has experienced (e.g. Ibata et al. 2007), however far more detailed study of remote M31 members will be required to shed light on this possibility.

MGC1 offers a useful probe of the outermost regions of the M31 halo, where only a very few stars have previously been measured (Chapman et al. 2006, 2008; Kalirai et al. 2006; Koch et al. 2008). The metal abundance we derive for MGC1 is low, [Fe/H] ≈ −2.3. This is in contrast to the results from recent high-resolution spectroscopy by Alves-Brito et al. (2009), who found [Fe/H] = $-1.37 \pm 0.15$. The origin of this discrepancy is unclear, however, we note that it also exists for the other two clusters in their sample:

[6] Here, the factor $\pi/4$ scales the three-dimensional radius $R_{gc} = 40$ kpc to an average projected radius.

GC5 and GC10, which are the next two most remote known M31 clusters with $R_p = 78$ and 100 kpc. Alves-Brito et al. (2009) derive [Fe/H] $= -1.33 \pm 0.12$ and [Fe/H] $= -1.73 \pm 0.20$, respectively, for these objects, while high-quality CMDs suggest [Fe/H] $= -1.84 \pm 0.15$ and [Fe/H] $= -2.14 \pm 0.15$ (Mackey et al. 2007). Until these disagreements are resolved, it is too early to conclude that the mean globular cluster metallicity at large radii in M31 flattens off at [Fe/H] $\sim -1.6$ as suggested by Alves-Brito et al. (2009). Taking the CMD results at face value would instead indicate that [Fe/H] $\lesssim -2.0$ for clusters beyond $R_p \sim 80$ kpc.

The situation for M31 halo stars at radii beyond ∼70 kpc is, at present, confusing (see e.g. the discussion in Richardson et al. 2009). Spectroscopic studies by Kalirai et al. (2006) and Chapman et al. (2006, 2008) suggest $\langle$[Fe/H]$\rangle \sim -1.3$ in the range $60 \lesssim R_p \lesssim 160$ kpc, not inconsistent with the peak of the (photometric) metallicity distribution function (MDF) for outer halo non-stream stellar populations derived by Ibata et al. (2007). On the other hand, after re-analysing much of the spectroscopic data from the above studies, Koch et al. (2008) found that the mean metal abundance of M31 halo stars may fall below −2 beyond $R_p \sim 80$ kpc, and reach as low as $\langle$[Fe/H]$\rangle \sim -2.5$ at $R_p \sim 160$ kpc. The MDF of Ibata et al. (2007) appears to exhibit a metal-poor tail and our results for MGC1 suggest that there must be at least *some* very metal-poor component of the extremely remote outer halo of M31. However, on the whole it seems that the most distant globular clusters in M31 are more metal poor than the bulk of the field halo stars at comparable radii.

Another remarkable feature of MGC1 is its extremely extended outer structure. Cluster members are clearly visible at large radii, and these are apparently fairly homogeneously distributed azimuthally. We have traced the radial profile of MGC1 to at least ∼450 pc and possibly as far as ∼900 pc, rendering it by far the most extended globular cluster hitherto studied. The most extended cluster in the Milky Way is NGC 2419, with $r_t \approx 200$ pc; the vast majority of the Galactic population have $r_t \lesssim 100$ pc (e.g. Mackey & van den Bergh 2005). The unique structure of MGC1 likely reflects its unmatched remote location, away from any strong tidal forces which might act to impose a tight limit on its radial extent. The expected tidal radius of a globular cluster of mass $M_{cl}$ orbiting a galaxy of mass $M_g$ at a galactocentric radius $R_{gc}$ is given by

$$r_t = R_{gc} \left( \frac{M_{cl}}{3M_g} \right)^{1/3}. \quad (9)$$

Adopting our measured parameters for MGC1 ($R_{gc} = 200$ kpc and $L_{tot} = 4.05 \times 10^5\,L_\odot$) along with a typical $V$-band mass-to-light ratio (M/L), for a globular cluster $M/L \approx 2$ and the mass of M31 from Evans & Wilkinson (2000), $M_g \approx 1.2 \times 10^{12}\,M_\odot$, we find the expected tidal radius for MGC1 is $r_t \sim 1200$ pc. Therefore, it is not surprising we have not identified a tidal cut-off in its radial profile.

Note that we cannot be certain that the outermost cluster members are bound to the cluster, since any tidal distortions would not necessarily lie in the plane of the sky. However, the lack of any clear spatially asymmetric distribution of these outer members together with the calculation above showing a very large expected $r_t$ suggests more of a halo-type structure than strong tidal tails.

Assuming a bound halo of stars around the cluster, the observed power-law fall-off of the profile is not unexpected. Baumgardt, Hut & Heggie (2002) used $N$-body simulations to study the long-term evolution of isolated star clusters. Their models show that an isolated cluster tends to build up a surrounding halo of stars that have been scattered on to radial orbits by two- or three-body encounters in the inner regions of the cluster. The resulting density profile follows a power-law fall-off as $\rho \sim r^{-3.3}$ at large radii. This is very similar to the results from, for example, the Monte Carlo models of Spitzer (1987) which predict $\rho \sim r^{-3.5}$. In projection, we thus expect a power-law fall-off with an exponent somewhere between $-2.5 \lesssim \gamma \lesssim -2.3$, which is entirely consistent with what we observe for the inner profile of MGC1.

In both sets of models, the core-halo structure takes many median relaxation times to establish over radial ranges of up to $\sim 100 r_h \approx$ 750 pc for MGC1. It is therefore perhaps not surprising that we observe a break to a steeper fall-off in the outer regions of MGC1. This may reflect the ongoing initial build-up of the cluster's halo or possibly the re-establishment of this halo after the last pericentre passage of MGC1 which could have brought it much closer to M31 than it is at present. Whatever the case, given that the median relaxation time of MGC1 is likely to be several Gyr (see, e.g., the values listed for Galactic globulars by Harris 1996), the existence of a core-halo structure at all suggests that MGC1 has been evolving in isolation for a very considerable period of time.

## 6 CONCLUSIONS

In summary, we have presented resolved photometric measurements of MGC1 from deep Gemini/GMOS imaging of this remote M31 cluster. Our resulting CMD displays features consistent with those of an ancient stellar population, including a long HB populated across the instability strip. By fitting isochrones calculated by several different groups, as well as fiducial sequences observed for Galactic globular clusters, we determine MGC1 to be a metal-poor object with [M/H] $\approx -2.3$. This is in disagreement with a recent high resolution spectroscopic measurement by Alves-Brito et al. (2009) who find a significantly higher metal abundance; the origin of this discrepancy is not yet clear but it also exists for several other remote M31 globular clusters.

The best-fitting stellar evolution models and globular cluster fiducials suggest that MGC1 lies significantly closer to us than M31. Our preferred distance modulus is $\mu = 23.95 \pm 0.06$ (corresponding to a line-of-sight distance of ≈620 kpc), compared with the generally accepted value for M31 of $\mu_{M31} = 24.47$ (≈780 kpc). Combined with the large projected separation between MGC1 and M31 ($R_p = 117$ kpc), our distance measurement implies that MGC1 lies in the extreme outer regions of the M31 halo with a galactocentric radius $R_{gc} = 200 \pm 20$ kpc. This renders it the most isolated known globular cluster in the Local Group by some considerable margin. Even so, the radial velocity measured for this object (Galleti et al. 2007; Alves-Brito et al. 2009) is within the M31 escape velocity and consistent with that expected for an M31 halo member at the radius of MGC1.

By measuring the radial brightness profile of MGC1, we have established that this cluster is centrally concentrated with a core radius $r_c \approx 2$ pc. It is also rather luminous with $M_V = -9.2$. This reinforces the notion, first put forward by Mackey et al. (2007), that M31 possesses a population of compact, luminous globular clusters in its outer halo that does not have a counterpart in the Milky Way.

Perhaps unsurprisingly given its extremely remote location, MGC1 does not show any evidence for a tidal limit in its outer regions, and King models do not provide a good description of the shape of the brightness profile at large radii. Instead, we observe a power-law fall-off with exponent $\gamma = -2.5$, breaking to $\gamma = -3.5$ in the outermost parts. This core-halo structure, which we see extending to radii of at least 450 pc and possibly as far as ∼900 pc, is broadly in line with expectations derived from numerical modelling of isolated globular clusters. In this regard, MGC1 is unique

in our experience – the most radially extended globular cluster in the Milky Way is NGC 2419 which shows a tidal cut-off at $r_t \approx 200$ pc. Further detailed observational study of MGC1 may therefore be extremely useful for advancing our understanding of globular cluster evolution.

## ACKNOWLEDGMENTS

ADM and AMNF are supported by a Marie Curie Excellence Grant from the European Commission under contract MCEXT-CT-2005-025869. NRT acknowledges financial support via a STFC Senior Research Fellowship. This work is based on observations obtained at the Gemini Observatory, which is operated by the Association of Universities for Research in Astronomy, Inc., under a cooperative agreement with the NSF on behalf of the Gemini partnership: the National Science Foundation (United States), the Science and Technology Facilities Council (United Kingdom), the National Research Council (Canada), CONICYT (Chile), the Australian Research Council (Australia), Ministério da Ciência e Tecnologia (Brazil) and SECYT (Argentina). These observations were obtained under program GN-2007B-Q-58.

## REFERENCES

Alves-Brito A., Forbes D. A., Mendel J. T., Hau G. K. T., Murphy M. T., 2009, MNRAS, 395, L34
An D. et al., 2008, ApJS, 179, 326
Barmby P., Holland S., Huchra J. P., 2002, AJ, 123, 1937
Baumgardt H., Hut P., Heggie D. C., 2002, MNRAS, 336, 1069
Bilir S., Karaali S., Tunçel S., 2005, Astron. Nachr., 326, 321
Carney B. W., 1996, PASP, 108, 900
Clem J. L., Vanden Berg D. A., Stetson P. B., 2008, AJ, 135, 682
Chapman S. C., Ibata R., Lewis G. F., Ferguson A. M. N., Irwin M., McConnachie A., Tanvir N., 2006, ApJ, 653, 255
Chapman S. C. et al., 2007, ApJ, 662, L79
Chapman S. C. et al., 2008, MNRAS, 390, 1437
Dotter A., Chaboyer B., Jevremović D., Baron E., Ferguson J. W., Sarajedini A., Anderson J., 2007, AJ, 134, 376
Dotter A., Chaboyer B., Jevremović D., Kostov V., Baron E., Ferguson J. W., 2008, ApJS, 178, 89
Elson R. A. W., Fall S. M., Freeman K. C., 1987, ApJ, 323, 54 (EFF)
Evans N. W., Wilkinson M. I., 2000, MNRAS, 316, 929
Ferguson A. M. N., Irwin M. J., Ibata R. A., Lewis G. F., Tanvir N. R., 2002, AJ, 124, 1452
Fukugita M., Ichikawa T., Gunn J. E., Doi M., Shimasaku K., Schneider D. P., 1996, AJ, 111, 1748
Galleti S., Bellazzini M., Federici L., Buzzoni A., Fusi Pecci F., 2007, A&A, 471, 127
Girardi L., Bressan A., Bertelli G., Chiosi C., 2000, A&AS, 141, 371
Girardi L., Grebel E. K., Odenkirchen M., Chiosi C., 2004, A&A, 422, 205
Harris W. E., 1996, AJ, 112, 1487
Hook I., Jørgensen I., Allington-Smith J. R., Davies R. L., Metcalfe N., Murowinski R. G., Crampton D., 2004, PASP, 116, 425
Huxor A. P., Tanvir N. R., Irwin M. J., Ibata R. A., Collett J. L., Ferguson A. M. N., Bridges T., Lewis G. F., 2005, MNRAS, 360, 1007
Huxor A. P., Tanvir N. R., Ferguson A. M. N., Irwin M. J., Ibata R. A., Bridges T., Lewis G. F., 2008, MNRAS, 385, 1989
Huxor A. P. et al., 2009, MNRAS, submitted
Ibata R., Irwin M., Lewis G., Ferguson A. M. N., Tanvir N., 2001, Nat, 412, 49
Ibata R., Martin N. F., Irwin M., Chapman S., Ferguson A. M. N., Lewis G. F., McConnachie A. W., 2007, ApJ, 671, 1591
Irwin M., Lewis J., 2001, New Astron. Rev., 45, 105
Jester S. et al., 2005, AJ, 130, 873
Jordi K., Grebel E. K., Ammon K., 2006, A&A, 460, 339
Jorgensen I., 2009, PASA, 26, 17
Kalirai J. S. et al., 2006, ApJ, 648, 389
King I., 1962, AJ, 67, 471
Koch A. et al., 2008, ApJ, 689, 958
Landolt A. U., 1992, AJ, 104, 340
Mackey A. D., van den Bergh S., 2005, MNRAS, 360, 631
Mackey A. D. et al., 2006, ApJ, 653, L105
Mackey A. D. et al., 2007, ApJ, 655, L85
McConnachie A. W., Irwin M. J., Ferguson A. M. N., Ibata R. A., Lewis G. F., Tanvir N., 2005, MNRAS, 356, 979
McConnachie A. W. et al., 2009, Nat, 461, 66
Marigo P., Girardi L., Bressan A., Groenewegen M. A. T., Silva L., Granato G. L., 2008, A&A, 482, 883
Martin N. F., Ibata R. A., Irwin M. J., Chapman S., Lewis G. F., Ferguson A. M. N., Tanvir N., McConnachie A. W., 2006, MNRAS, 371, 1983
Pietrinferni A., Cassisi S., Salaris M., Castelli F., 2004, ApJ, 612, 168
Pietrinferni A., Cassisi S., Salaris M., Castelli F., 2006, ApJ, 642, 797
Richardson J. C. et al., 2009, MNRAS, 396, 1842
Salaris M., Chieffi A., Straniero O., 1993, ApJ, 414, 580
Sarajedini A., 1994, AJ, 107, 618
Schlegel D. J., Finkbeiner D. P., Davis M., 1998, ApJ, 500, 525
Spitzer L., 1987, Dynamical Evolution of Globular Clusters. Princeton Univ. Press, Princeton, NJ
Stetson P. B., 1987, PASP, 99, 191
Stoughton C. et al., 2002, AJ, 123, 485
Tanvir N. R. et al., 2009, MNRAS, submitted
Tucker D. L. et al., 2006, Astron. Nachr., 327, 821
van den Bergh S., Mackey A. D., 2004, MNRAS, 354, 713

This paper has been typeset from a TEX/LATEX file prepared by the author.